Sensors & Actuators: B. Chemical 425 (2025) 136875

Contents lists available at ScienceDirect

Sensors and Actuators: B. Chemical

journal homepage: www.elsevier.com/locate/snb

# Optimized sensing on gold nanoparticles created by graded-layer magnetron sputtering and annealing

Deshabrato Mukherjee [a,b], Krisztián Kertész [a], Zsolt Zolnai [a], Zoltán Kovács [a], András Deák [a], András Pálinkás [a], Zoltán Osváth [a], Dániel Olasz [a,c], Alekszej Romanenko [a,d], Miklós Fried [a,b], Sven Burger [e], György Sáfrán [a], Péter Petrik [a,f,*]

[a] Institute of Technical Physics and Materials Science, HUN-REN Centre for Energy Research, Konkoly Thege Str. 29–33, Budapest, 1121, Hungary
[b] Doctoral School of Materials Sciences and Technologies, Óbuda University, Népszínház u. 8, Budapest, 1081, Hungary
[c] Department of Materials Physics, Eötvös Loránd University, Pázmány Péter Sétány 1/A, Budapest, 1117, Hungary
[d] Doctoral School of Chemistry, Eötvös Loránd University, Pázmány Péter sétány 1/A, Budapest, H-1117, Hungary
[e] Zuse Institute Berlin (ZIB) & JCMwave GmbH, Takustraße 7, Berlin, 14195, Germany
[f] Department of Electrical Engineering, Institute of Physics, Faculty of Science and Technology, University of Debrecen, Bem tér 18, Debrecen, 4026, Hungary

ARTICLE INFO

*Keywords:*
Gold nanoparticle
Localized surface plasmon
Sensors
Gas sensing
Finite element electromagnetic simulation
Sensing optimization

ABSTRACT

Graded-thickness gold layers were deposited on fused silica by combinatorial magnetron sputtering and annealing to form nanoparticles with a laterally changing structure. The optical properties and sensing characteristics were determined as a function of the amount of sputtered material by scanning optical spectroscopies. The formation and sensing performance of Au nanoparticles were modeled and interpreted by finite element electromagnetic calculations. The most sensitive regions for the optical detection of ethanol, water, and Raman reporter molecules on the heat-treated surfaces were determined as a function of the deposited amount of Au. For all three analytes applied, we observed the best sensing performance for an effective deposited gold thickness of 2–3 nm. These results can be interpreted by considering the graded gold film's actual geometry and near-field optical properties.

## 1. Introduction

Gold nanoparticles (GNPs) possess unique optical, electronic, and catalytic properties, making them ideal for nanoscale devices. Gold has become increasingly popular in preparing nanosized devices due to its many desirable properties, including high conductivity, biocompatibility, and ease of synthesis. This has resulted in their usage in a wide range of applications such as bioimaging, drug delivery, sensing [1], theranostics [2], hot electron science [3–5], thermoplasmonics [6,7], and catalysis [8]. In nanoelectronics, GNPs have been used as components [9] in electronic devices such as transistors, memory devices, and sensors.

The unique optical properties of GNPs have also been exploited in developing plasmonic devices for sensing [1,10–12] and imaging applications. For an isolated metal surface, a surface plasmon wave cannot be excited directly (a grating, prism, or sharp geometric features are needed to conserve energy and k-vector). The interaction of the surface plasmon wave with the biomolecules at the metal surface is detected using surface plasmon resonance (SPR) [13]. The change of the refractive index ($n$) of the medium is detected as a shift in one of the SPR parameters such as the angle [14], wavelength [15,16] or other resonance parameters [17]. Hot carriers [5,18] have also been utilized in such processes for varied applications [19].

When incident light interacts with metallic nanoparticles such as gold, typically in the range of 5–100 nm in size, it results in a phenomenon called localized surface plasmon resonance (LSPR), where electrons collectively oscillate on the nanoparticle surface. This oscillation can be tuned to specific wavelengths of light ($\lambda$) by varying the size, shape, and surface chemistry of the GNPs [20]. Accordingly, the LSPR is highly sensitive to the local environment of the GNPs, including the (anisotropic) permittivity tensor ($\epsilon$) [21] and the proximity of nearby molecules. The size and shape of the nanoparticle, along with these factors mentioned above, play a decisive role in the $\lambda$ at which LSPR occurs. Thus, adjusting the GNPs' properties and the local environment becomes critical in modulating the LSPR signal, leading to increased sensitivity, spatial resolution, and lower detection limits.

LSPR can be effectively utilized for a large variety of sensing purposes (chemical sensors, gas sensors [22–24], biosensors [25,26],

* Corresponding author at: Institute of Technical Physics and Materials Science, HUN-REN Centre for Energy Research, Konkoly Thege Str. 29–33, Budapest, 1121, Hungary.
*E-mail address:* petrik.peter@ek.hun-ren.hu (P. Petrik).

https://doi.org/10.1016/j.snb.2024.136875
Received 2 August 2024; Received in revised form 23 October 2024; Accepted 30 October 2024
Available online 14 November 2024

etc.) [27–31] by measuring changes in $n$ of the surrounding media with high sensitivity, often using ellipsometry [32]. Such optical sensor elements can be sensitive enough to be used in biosensors for monitoring/recognition of molecular scale interactions [31]. GNPs are particularly well suited for LSPR-based sensing due to their tunable optical response in the visible to near-infrared range. Applications of LSPR-based sensing using GNPs include the detection of small molecules, proteins, and even viruses, e.g., GNPs have been used to detect the presence of cancer biomarkers in blood [33–35], or bacteria in water [36–39]. In addition, GNP-based LSPR has also been used in Surface-Enhanced Raman spectroscopy (SERS) [2,40] for analyte detection at the molecular level.

There are various different approaches to prepare plasmonic nanoparticles for sensing including bulk chemical [11], electrochemical [41], physical deposition [15,42–45], self-assembly [24], the formation of nanoaggregate containers [46] or porous nanoparticles [47], ordered adsorption, holographic methods [48], colloid chemistry [49–53], ligand-controlled assembly [54], nanosphere assembly [55,56] and lithography [57], composites with polymers [58], combination with other plasmonic [59] or 2D materials [60], electron beam lithography or ion beam methods [31]. Each method has its advantages in terms of cost, speed, reliability, sensitivity, adjustability, etc. The sputter deposition process utilized in this work finds application for fabricating discontinuous multilayer thin films [61]. There is an evident change in the $Au/SiO_2$ optical response caused by changes in system morphology, which progresses from cluster-like systems with GNPs dispersed on the silica surface to island-like structures with Au aggregates partially interconnected. Controlling the distribution and surface concentration of GNPs is thus a critical step in developing plasmonic nano-systems with well-tuned optical characteristics [62]. Thermally driven generation of gold nanoparticles for optical sensing has several advantages. (i) It is simple, requiring only a thin gold layer's deposition and subsequent annealing at a few hundred °C [16,63,64]. (ii) The LSPRs can be optically generated in simple transmission cells, avoiding the application of the Kretschmann–Raether configuration [43,65,66]. (iii) Gold is stable with no formation of a surface oxide layer. (iv) The combinatorial approach can efficiently be utilized in thin film technology [67]. This process finds application even for the fabrication of discontinuous multilayer thin films [61,68], and it may even be possible to quickly and reproducibly scale up the production.

These structures' physical and chemical properties have been investigated extensively [16]; however, the optical and sensing features largely depend on the preparation parameters [69], most significantly on the amount of deposited material before annealing. The gradient deposition method [70,71] used in this study not only provides a tool to ascertain the influence of the initial thickness deposited, but it can also be a powerful concept, which enables that the location of highest sensitivity can be found even in case of run-to-run deviations in the sample preparation. This can be critical if the tolerance for the sample parameters is small.

## 2. Experimental details

The graded-thickness Au layer was deposited on UV-grade fused silica Corning glass substrates of dimensions 25 mm × 10 mm × 0.15 mm (length × width × thickness) purchased from Valley Design Corp. Before deposition, the substrates were cleaned in methanol, acetone, and ultrapure milli-Q water. A combinatorial device and variable power DC magnetron sputtering were used to create the Au layers with a thickness changing gradually from zero to 20 nm along the long edge of the sample over a lateral distance of either 25 mm (sample 'A') or 20 mm (sample 'B') [70]. In the case of sample 'B,' the gold-covered region is centered on the slide, i.e., there are uncovered regions of 2.5 mm at both ends. In the graphs shown after this, the lateral position ($X_l$) is also referred to as the nominal equivalent thickness (effective or mass thickness [72]) of the gold layer denoted by $d_i$. In the regions of nanoparticles, $d_i$ is the thickness of the layer that contains the deposited amount of material in a homogeneous form.

In the combinatorial deposition process shown in Fig. 1a, a shutter with a slit (2) is moving above the substrate (3), where gold (4) is deposited from the DC magnetron source (1) with variable power synchronized to the position of the slit. This method allows the preparation of arbitrary thickness profiles and compositions when two sources are applied parallelly [70], and our group has previously shown that linear composition profiles can accurately be created using this technique [71]. In the present case, there is only a single element deposited; however, the method ensures that the amount of deposited material is linearly proportional to the lateral position measured on the substrate, which opens up innumerable opportunities for the controlled preparation of plasmonic and resonant alloys [45,73].

Sample 'A' was investigated by a homemade tool, a scanning optical reflection, and a transmission spectrometer. The setup uses an Avantes AvaSpec-HSC1024 × 58TEC-EVO modular fiber optic spectrometer and an AvaLight-DH-S-BAL light source. As illustrated in Fig. 1b, the fiber from the light source (1) illuminates the sample (3) through a quartz glass cell (2), and the fiber collecting the transmitted light (4) is connected to the spectrometer. For ethanol vapor sensitivity measurements, we let flow synthetic air (80% $N_2$, 20% $O_2$) through the cell at 1 l/min rate with the possibility of ethanol vapor addition from a gas bubbler [74]. Identical concentrations of ethanol vapor were inserted in the glass cell for 30 s, and the optical transmittance change was measured and saved over time at different locations of the sample.

The layer structure and thickness as a function of $X_l$ were measured by a Woollam M-2000DI rotating compensator spectroscopic ellipsometer. $\Psi$ and $\Delta$ spectra were measured, where $r_p/r_s = \tan(\Psi)\exp(i\Delta)$. Here, $r_p$ and $r_s$ denote the complex reflection coefficients of light polarized parallel and perpendicular to the plane of incidence, respectively. The ellipsometry measurements are visualized by plotting the $m_{33} = \tan(2\Psi)\cos(\Delta)$ Mueller matrix parameter that describes the transformation of $I_{+45} - I_{-45}$ intensity differences during the interaction with the sample ($I_{+45}$ and $I_{-45}$ denote intensity values of light with polarization rotated plus and minus 45 degrees with respect to the plane of incidence). Furthermore, the $m_{33}$ parameter (which can also be interpreted as the diagonal element corresponding to the $S_2$ Stokes parameter) includes both phase and amplitude information, which is included in a trigonometric function that eliminates phase jumps.

Using a focused spot of 0.3 mm nominal diameter, the corresponding thickness resolution is estimated to be between 0.24 and 0.30 nm. Whereas the dotted line in Fig. 1c shows the mass thickness ($d_i$) corresponding to the deposited amount of material known from the calibrated sputter rate, the red circles plot the thickness measured by ellipsometry modeling the raw spectra shown in Fig. 1h by a simplified optical model of Au/glass using references of Au [75] and 'fused silica' from the database of the ellipsometer. Here, the 'Error of fit' curve shows the validity of the uniform Au layer model, i.e., the unitless values of the square root of the sum of differences between the measured and calculated values normalized to the standard deviations of the measurement at each spectral point. Note that for positions below 2.5 mm, the error of fit is low as there was no Au deposited on the surface (and it was not considered in the fits as well). The increase in the error of fit above positions of 2.5 mm clearly shows the presence of gold nanoparticles, i.e., a discontinuous Au film already for the as-deposited sample. The increased error of fit in this region is because the uniform model cannot describe the GNP structure. The uniform layer model works well only from the lateral position at which the error drops to nearly zero, which is close to $X_l = 9$ mm in agreement with other studies [76]. This location corresponds to a mass thickness of $d_i = 6.5$ nm on sample 'B', and thus may correspond to the formation of a continuous gold film. The fact that the thickness determined from the fit using the uniform single-layer model (red dots in Fig. 1c) is below $d_i$ (dotted line) and it meets the zero axis at the position of $X_l = 5$ is because the optical model in this region is not suitable for

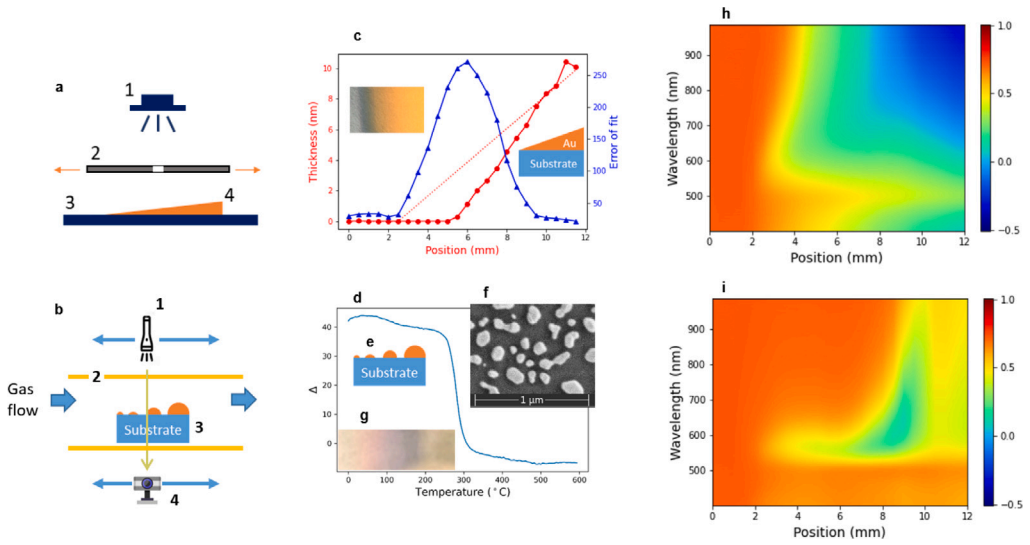


**Fig. 1.** (**a**) Schematic view of the micro-combinatorial sputtering method [70] including the (1) magnetron sputtering source, (2) the moving slit, (3) the substrate, and (4) a schematic graded-thickness gold layer deposited by sputtering. (**b**) Configuration of the optical transmission cell with (1) the light source, (2) the glass chamber, (3) the sample with thermally generated graded nanoparticles on a substrate, and (4) the spectrometer. (**c**) Thickness (red circles), effective thickness (also called 'mass thickness' [72]) corresponding to the deposited amount of material (dotted line), and error of fit for the as-deposited graded Au sample 'B' measured by ellipsometry. (**d**) Change of $\Delta$ measured by ellipsometry as a function of temperature during annealing at the $\lambda = 632.9$ nm and position of 8 mm on sample 'B.' (**e**) Schematic, (**f**) scanning electron microscopy (at a position of 8 mm), and (**g**) optical images on the sample after annealing. (**h**) and (**i**) show $m_{33}$ spectra on sample 'B' over the range of positions from 0 to 12 mm for the as-deposited and 300 °C annealed state, respectively.

the calculation, and the result is not acceptable. Working out suitable optical models for the ellipsometry measurements on Au NPs is a topic of a separate publication, based on the numerous approaches available in the literature [49,50,72].

The samples were annealed using a gradually increasing temperature of 2 °C/min up to 600 °C. Fig. 1d shows the $\Delta$ value measured by ellipsometry during annealing, revealing that the transition temperature was reached during annealing and that there is no more substantial change at temperatures above 300 °C. Figs. 1h and 1i reveal the significant changes over the whole range, also at locations where the layer was non-homogeneous (island-like) already before annealing. The appearance of the plasmon-related peaks can be seen between $\lambda = 550$ - 600 nm for locations between 2.5 mm (the beginning of the deposition) and $\approx 8$ mm that spectrally broadens towards higher $\lambda$ values between the positions of $\approx 8$ and 10 mm ($d_i = 5.5 \rightarrow 7.5$ nm).

The morphology of the nanoparticles (Fig. 2) was analyzed using a Zeiss Supra Scanning Electron Microscope (SEM) at an acceleration voltage of 5 kV. The images were analyzed using the OpenCV python library and the ImageJ open-source software. Numerical simulations of the optical response of the nanostructures were performed using JCMsuite, a time-harmonic finite element (FEM) solver. Inelastic light scattering measurements were performed using a WITec confocal Raman microscope at excitation wavelengths of $\lambda = 532$ and 633 nm with a laser spot size of less than 1 µm$^2$. Single Raman spectra were acquired at different distances from the sample edge (in steps of 0.2 mm), and each spectrum accumulated for 25 s.

4-mercaptobenzoic acid (MBA) Raman reporter molecules were adsorbed to the Au surface in the aqueous bulk phase. MBA is well suited for testing the structure's SERS performance due to its characteristic vibrations and ability to form Au-S covalent bonds between the analyte molecules and the Au surface atoms [17]. The analyte-treated sample was prepared by immersing the substrate into 25 mM ethanolic solution of MBA overnight, followed by rinsing with ethanol, and finally dried by exposure to air. Ellipsometry was also used to measure the change of ellipsometry angles due to MBA and water adsorption. For the sensing of water adsorption, the sample surface was cooled by a Peltier cell. The cooling was moderated in small steps to perform a full scan over the surface of the glass slide for all temperatures and adsorption states.

## 3. Results and discussion

SEM images reveal a densely packed nanoparticulate gold structure corresponding to the first few millimeters of lateral position on the glass substrates (Figs. 2a–c). The surface density of gold particles ($N$) is between 2000 and 2500 µm$^{-2}$ in the lateral positions below $\approx 3$ mm (Fig. 2g), which corresponds to a nominal initial layer thickness of $d_i \approx 2.5$ nm. Since the power of the sputter source is synchronized to the position of the slit along the substrate, i.e., to $X_l$, the volume ($V$) of sputtered material is strictly linear with $X_l$ starting from $d_i = 0$ nm at $X_l = 0$ mm to $d_i = 20$ nm at $X_l = 25$ mm, as it is verified by ellipsometry. Therefore, the range of positions ($X_i = 1.5 \rightarrow 7.5$ mm) shown in Figs. 2g and 2h corresponds to a nominal initial layer thickness range of $d_i = 0.8 \rightarrow 6$ nm. The surface density drops quickly, changing from 2090 µm$^{-2}$ at $d_i = 2$ nm to 88 µm$^{-2}$ at $d_i = 4.4$ nm, with a simultaneous decrease of the ratio of covered area ($f_c$) from 0.49 to 0.21 in the same positions. This change in the covered area agrees with the results reported in Ref. [77]. The $f_c$ saturates at a value close to 0.2 for $X_l > 4$ mm (Fig. 2g), while the equivalent average radius ($R$) of the nanoparticles shows a monotonous increase with $X_l$ (Fig. 2h). The height/radius ratio ($h/R$) is also plotted in this graph, with the $h$ calculated from the equivalence of the deposited volume ($V_d = d_i A_u$, where $A_u$ denotes the unit area) and the total volume of material contained in the nanoparticles ($V = N A_p h$, where $A_p$ denotes the average area per nanoisland and $h$ denotes the average height of the nanoisland). The analysis shows that the $h/R$ ratio gradually increases for positions below $\approx 4$ mm and is nearly constant above. Thus, the typical particle shape changes from oblate to hemispheroidal-like with increasing lateral sample positions. The almost constant $h/R$ ratios above the positions of $\approx 4$ mm suggests that in this region, a nearly similar (hemi) spherical shape can be assumed for the GNPs formed after annealing. Note the abrupt increase of the estimated effective interparticle gap for lateral sample positions above $\approx 3$ mm in Fig. 2h. The gap width is a key factor in the near-field coupling of adjacent plasmonic nanoparticles since small gaps are favorable in local electric field intensification processes [77] for enhanced Raman scattering of probe molecules located in the gap region.

The optical reflectance spectra were measured using the tool shown in Fig. 1b on sample 'A' with a bifurcated fiber optic normal to the

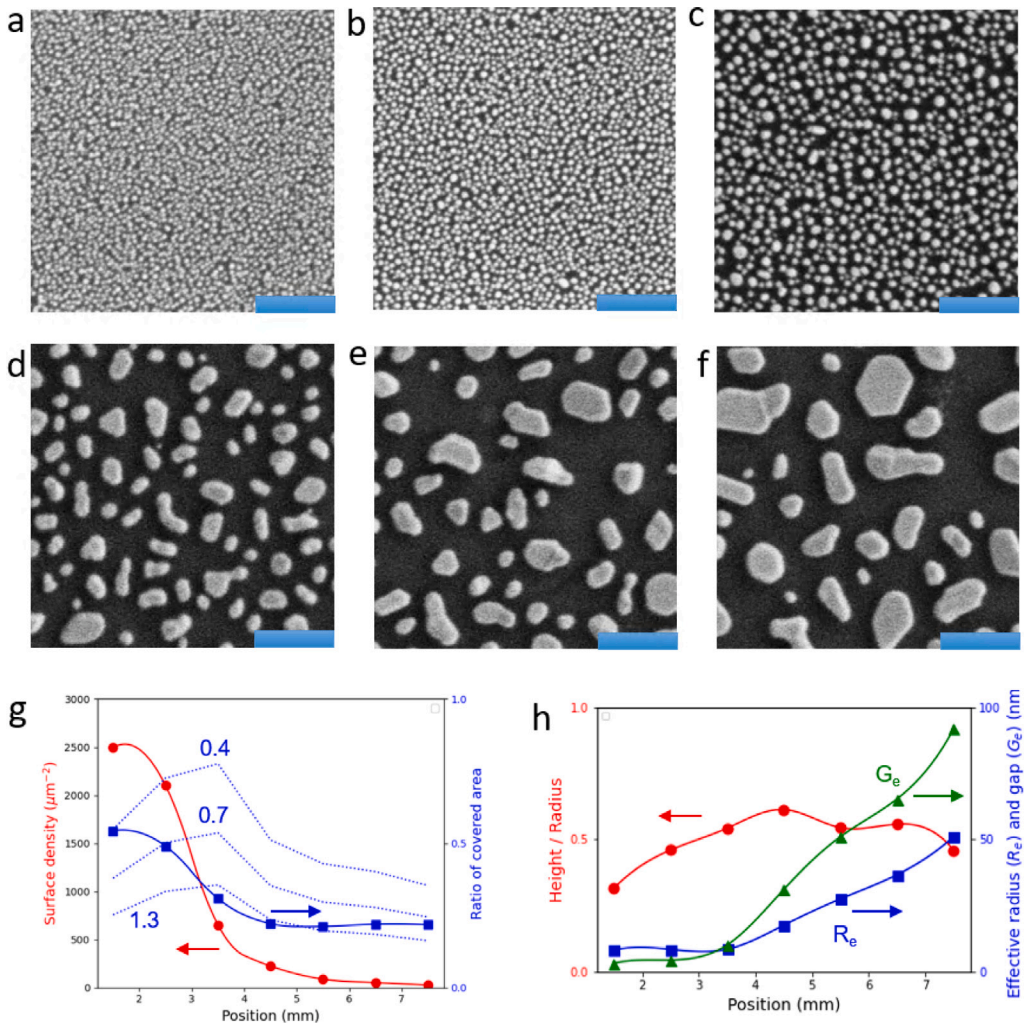


**Fig. 2.** (**a**)–(**f**) SEM images of thermally treated gold nanoparticles in sample 'A' at lateral positions ($X_l$) of 1.0, 2.5, 3.5, 5.5, 6.5, and 7.5 mm measured along the substrate, corresponding to mass thicknesses ($d_i$) of 0.8, 2.0, 2.8, 4.4, 5.2, and 6.0 nm, respectively. The blue scale bars are 200 nm long in each case. (**g**) Number of gold nanoparticles per μm$^2$ (red circles) and the ratio of the area covered by Au vs. lateral position (blue squares) on the substrate, with the dashed curves showing the ratio of the covered area for $h/R = 1.3, 0.7$ and 0.4. (**h**) Height/radius ratio (red circles) as well as the effective radius ($R_e$, blue squares) of the nanoparticles, and effective inter-particle gap ($G_e$, green triangles) as a function of the lateral position on the substrate. The solid lines are guides for the eye. The standard deviation of the GNP dimensions and the assumed error in graphs (**g**) and (**h**) is ≈ 10%.

sample scanning through the surface (Fig. 3a). In agreement with the ellipsometry results on sample 'B' (see Fig. 1i), the LSPR related peaks appear already at $X_l = 4$ mm ($d_i = 3.2$ nm), which broadens towards larger $\lambda$ values as $X_l$ increases. The most substantial LSPR related peak was measured at $X_l = 8.5$ mm ($d_i = 6.8$ nm), while the plasmons seem to be canceled above $X_l \approx 9.5$ mm ($d_i = 7.6$ nm). This is probably due to the vanishing separation between the nanoparticles accompanied by a more bulk-like behavior and, consequently, fading out of the LSPR oscillations. This trend was investigated by FEM, assuming the equivalence of the deposited volume $V_d = d_i g^2$ and the total volume $V_i = (4/3)R^3\pi/2$ in the nanoparticles. In the calculation shown in Fig. 3b, $R = 21$ nm was used as the value that most accurately reproduced the measurement (Fig. S1), and $g$ was set as the lateral size of the unit cell in FEM for each $X_l$ knowing the value of $d_i$. The effect of the aspect ratio and the dependence of $R$ on $X_l$ was also investigated, revealing that the measured plasmonic features can also be reproduced by assuming an increasing $R$ and an $h/R$ aspect ratio below 0.4; see the $R = 12 \rightarrow 48$ nm and $h/R = 0.4$ case in Fig. S2. In the models with aspect ratios other than one, an elliptical shape is assumed (Figs. 3c and 3f). The size, shape, and dielectric environment have been demonstrated to affect the optical properties significantly [78–80], see also Fig. S2.

The gold nanoparticles' sensing capabilities were investigated using calculations and measurements utilizing optical techniques with a suitable spatial resolution to map the optical response to $X_l$ values and, more importantly, to the deposited amount of material ($d_i$). Figs. 3b and 3d show FEM calculations without (b) and with (d) a 2-nm overlayer with a refractive index dispersion of $n = 1.45 + 0.01/\lambda^2$ ($\lambda$ is in units of μm) based on the model shown in Fig. 3f.

The optical transmittance measurements during ethanol sensing were performed in the setup shown in Fig. 1b. Positions with comparable steps in peak intensities were identified and plotted in Fig. 4a. Identical concentrations of ethanol were flown through the cell while taking spectra continuously. Fig. S3 shows the spectra recorded in real-time while switching the ethanol vapor flow for 30 s, before and after only the synthetic air is flowing. The dynamics of both the decreasing and increasing signals can be followed in the whole spectra for the on and off states of the vapor flow, respectively. The maximum drop in intensity during sensing in Fig. 4b is plotted for the positions labeled by numbers. The largest sensitivity can be identified for $d_i \approx 3.5$ nm at position Nr. 5. The wavelengths of the minimum positions (blue triangles) show an increasing trend with an increasing slope above $d_i \approx 5$ nm. The spots with thicker layers tend to be associated with slightly higher wavelengths, indicating the shift of the localized plasmon peaks to higher wavelengths with the increase in layer thickness and the decrease in transmission sensitivity. This is close to the highest

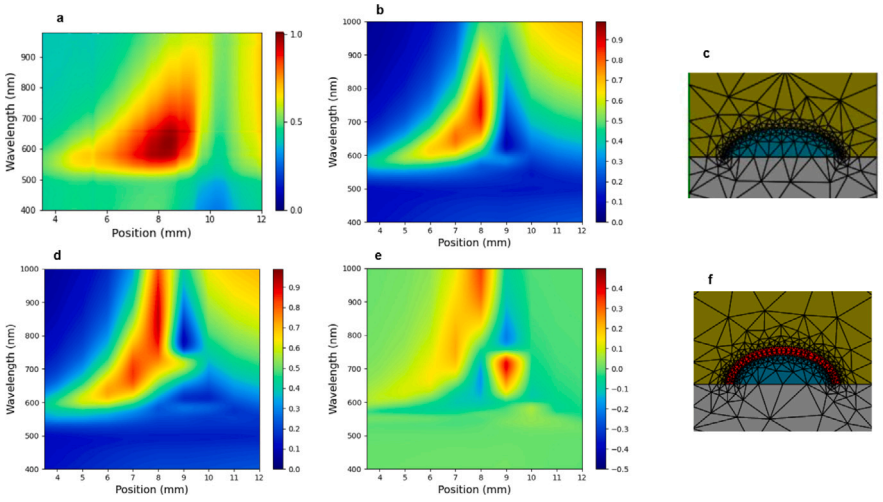


**Fig. 3.** (**a**) Reflectance spectra measured along Sample 'B' and (**b**) simulated at normal incidence using (**c**) a FEM model. (**d**) Reflectance spectra calculated for the same structure with (**f**) a model using an overlayer with a thickness of 2 nm and $n = 1.45 + 0.01/\lambda^2$, where the unit of $\lambda$ is in μm. The differences between (**b**) and (**d**) are plotted in (**e**). The parameters of $R$ and $h/R$ were set at $R = 21$ nm and $h/R = 0.8$ in each case.

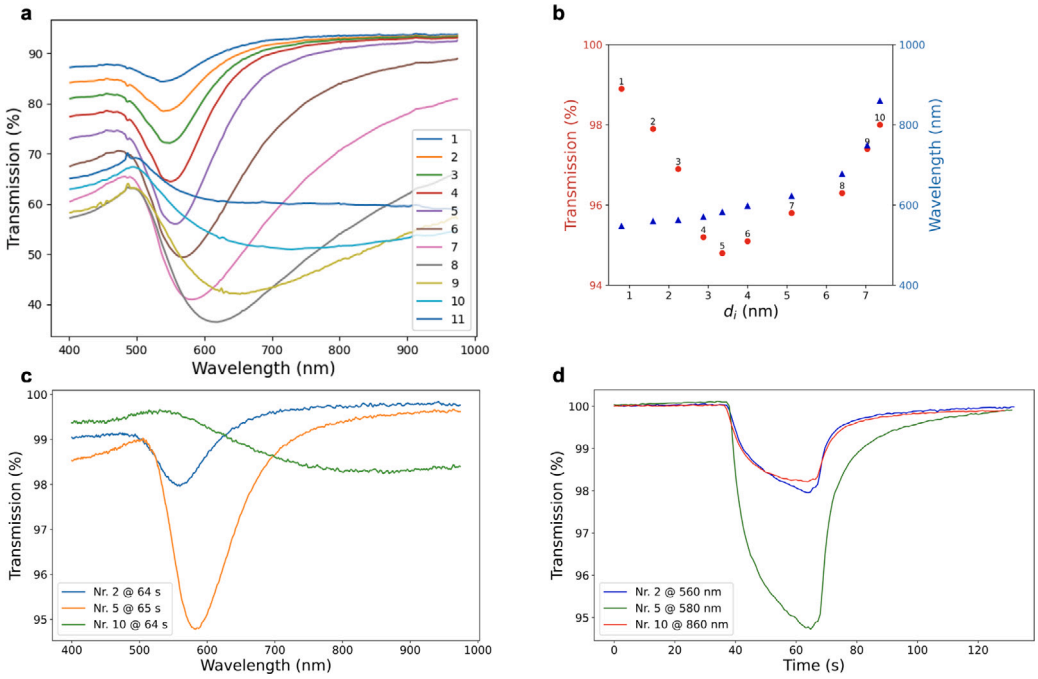


**Fig. 4.** (**a**) Transmission spectra normalized to the reference measured on the pure glass slide without an Au layer, for locations labeled as 1–10 in (**b**) which shows the transmission minima (denoted by red circles) and the corresponding wavelengths (denoted by blue triangles) during ethanol sensing (see Fig. S3). (**c**) Transmission spectra normalized to the spectrum recorded at $t = 0$ s for position 5. (**d**) Kinetics of the transmission signal at different sample positions (labeled as 2, 5, and 10), at specific wavelengths revealing the best dynamics.

sensitivity position measured by ellipsometry during water adsorption (Fig. 5c).

In Fig. 4d, we observe the change of the transmission percentage normalized to the $t = 0$ s spectrum with respect to time for three different spots, measured at specific wavelengths: Nr. 2 at 560 nm (blue line), Nr. 5 at 580 nm (green line), and Nr. 10 at 860 nm (red line) corresponding to the largest changes in transmission. After the onset of ethanol at $t = 40$ s the curves follow a saturating kinetics. The lateral position corresponding to the largest change of absorption is Nr. 5 at $X_l = 4$ mm ($d_i = 3.2$ nm). This coincides with the highest sensitivity position measured using ellipsometry during water adsorption and the transition region from high to low surface density and high to low surface coverage of gold nanoparticles shown in Fig. 2g. Nr. 2 (560 nm) and Nr. 10 (860 nm) exhibit a less profound dip compared to Nr. 5, with transmission falling slightly below 97. At $X_l = 4$ mm, the recovery gradually extends beyond the 60-second mark, suggesting prolonged interactions or changes, while in the case of Nr. 2 and Nr. 10, the recovery phase is faster, indicating a shorter interaction duration or faster stabilization.

A different behavior can be observed for MBA molecules covalently bonded to the surface, as measured by ellipsometry (Fig. 5a). This trend is also reproduced by simulations in Figs. 3d and 3e. The observed difference indicates that in the case of ethanol and water sensing, the molecules do not uniformly cover the surface thus contrary to the case of the covalently bonded MBA molecules.

The positions of highest Raman sensitivity (Figs. 5b and 5d) on the MBA-covered samples are different from those measured by ellipsometry (Fig. 5a). In the case of Raman sensing it is around 1–2 mm

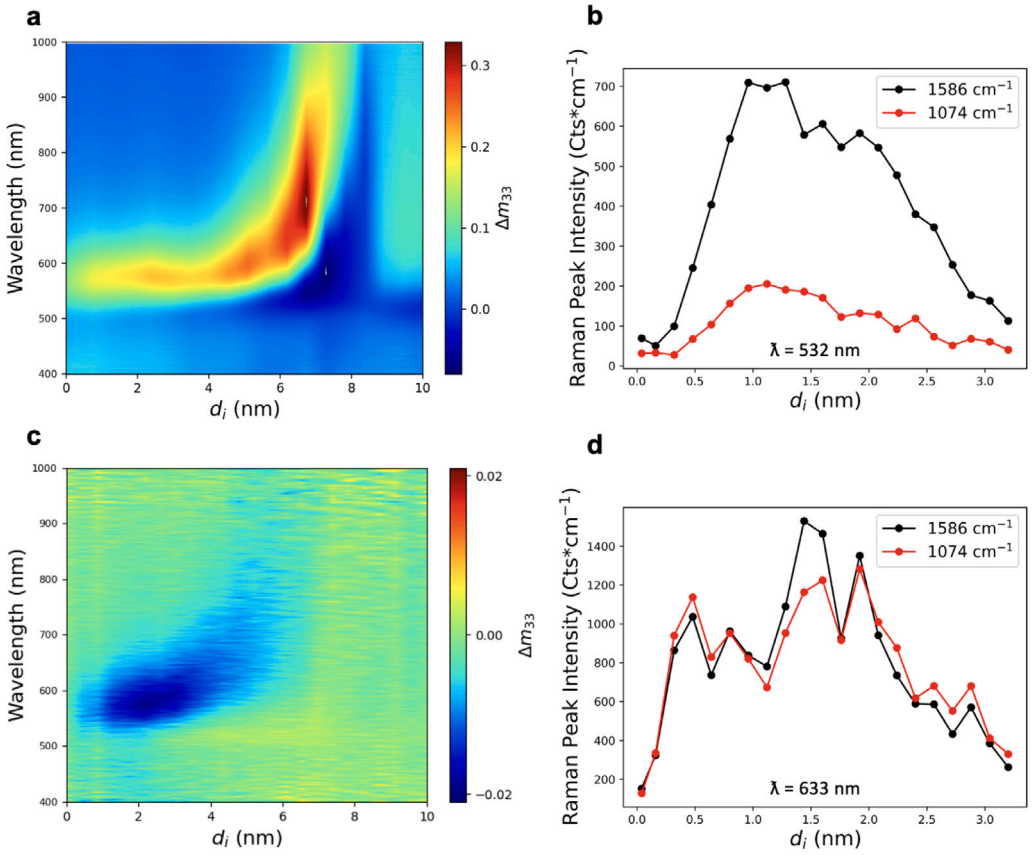


**Fig. 5.** (**a**) Differential values of the $m_{33}$ Mueller matrix element measured by ellipsometry at the angle of 70° before and after MBA and (**c**) water molecule adsorption. (**b**) and (**d**) shows the areas of the Raman peaks appearing at two different wavenumbers on sample 'A' for both 532 nm and 633 nm excitation wavelengths, respectively.

from the wafer's edge for both excitation wavelengths and MBA-related Raman peaks appearing at 1074 cm$^{-1}$ and 1586 cm$^{-1}$. Nevertheless, the high peak sensitivity region of the Raman measurement is close to that of the optical gas sensing positions of Figs. 4b and 5c. This region ($d_i$ = 1.6 nm) of the sample is clearly in the range of the highest surface density of gold nanoparticles and the highest ratio of covered surface area (Fig. 2g). Also, this region can be described with small interparticle gaps of a few nm (see Fig. 2h), and accordingly, with significant near-field coupling between adjacent gold particles leading to considerable local electric field intensification beneficial for Raman scattering enhancement [77]. Although in our case detailed calculations were not performed for such parameters, we refer to the results of 3D-FDTD simulations reported in Ref. [77], which show local electric field intensity enhancements of ≈ $10^3$, and thus SERS enhancement factors of ≈ $10^6$, at the plasmon resonance frequency, for an ensamble of hemispherical gold nanoparticles with surface coverage of ca. 60% and small interparticle gaps of a few nanometres. The resonance wavelength of the system in our case appears at around 570 nm (see Figs. 4b and 5a), for the positions of maximum Raman intensities, that is in consistence with the plasmon resonance frequency reported in Ref. [77] for nanoparticulate gold films with comparable geometry.

This sample region 1–2 nm from the wafer's edge dominates Raman scattering for both excitation wavelengths of 532 nm (Figs. 5b and S5a) and 633 nm (Figs. 5d and S5b), although for 532 nm excitation, a broad background is visible (Fig. S5a), which is missing for the 633-nm case (Fig. S5b). On the other hand, there is a striking difference in the Raman scattering intensities corresponding to the wavenumbers of 1074 cm$^{-1}$ and 1586 cm$^{-1}$ for excitation at 532 nm, while at the laser wavelength of 633 nm, similar peak intensities can be observed. These trends suggest differences in plasmon in-resonance conditions upon excitation, i.e., difference in SERS enhancement processes for the two characteristic Raman lines when the laser wavelength is switched from 532 nm to 633 nm. Selective Raman enhancement was also reported for, e.g., graphene [81] and $MoS_2$ [82] sheets as SERS probes settled in plasmonic nanostructures.

## 4. Conclusions

To optimize the plasmonic properties for molecule sensing, Au nanoparticles with progressively varying properties were created on fused silica substrates by DC magnetron sputtering followed by annealing. Using a gradient (combinatorial) technique, the amount of deposited material linearly changed with the position measured along the substrate. Scanning optical spectroscopies were used to characterize the optical and sensing properties as a function of equivalent deposited thickness $d_i$. The best gas sensing (Figs. 4b and 5c) positions were found for $d_i$ values of 2–4 nm, explained by the high surface density of gold particles and the high ratio of covered area in this region. The covalently bonded MBA molecules can most sensitively be detected at the highest plasmon peak region of $d_i$ ≈ 7 nm when using ellipsometry (Fig. 5a). However, the most sensitive region for the Raman measurement of the MBA molecules is at $d_i$ ≈ 1.6 nm (Figs. 5b and 5d). The formation and sensing performance of the layers were modeled and explained using finite element calculations. We have shown that our combinatorial sputtering method for arbitrary thickness and composition profiles can accurately and quickly locate optimal sensing parameters. It supports the discussion of theoretical and experimental considerations due to the large amount of data generated by quick optical scanning. It is suitable for the high throughput testing of new materials and structures and for creating experimental databases for theoretical analysis and machine learning.

## CRediT authorship contribution statement

**Deshabrato Mukherjee:** Writing – review & editing, Writing – original draft, Visualization, Validation, Software, Methodology, Investigation, Formal analysis, Data curation. **Krisztián Kertész:** Writing – review & editing, Writing – original draft, Visualization, Validation, Investigation, Formal analysis, Data curation, Conceptualization. **Zsolt Zolnai:** Writing – review & editing, Writing – original draft, Validation, Methodology, Investigation, Formal analysis, Conceptualization. **Zoltán Kovács:** Software, Investigation, Formal analysis, Conceptualization. **András Deák:** Writing – review & editing, Validation, Methodology, Investigation, Formal analysis, Data curation. **András Pálinkás:** Writing – review & editing, Visualization, Methodology, Investigation, Formal analysis, Data curation. **Zoltán Osváth:** Writing – review & editing, Validation, Methodology, Investigation, Formal analysis, Data curation. **Dániel Olasz:** Writing – review & editing, Methodology, Investigation, Formal analysis, Data curation. **Alekszej Romanenko:** Validation, Methodology, Investigation, Formal analysis, Data curation. **Miklós Fried:** Resources, Project administration. **Sven Burger:** Writing – review & editing, Methodology, Investigation, Formal analysis, Data curation. **György Sáfrán:** Writing – review & editing, Validation, Resources, Methodology, Investigation, Conceptualization. **Péter Petrik:** Writing – review & editing, Writing – original draft, Visualization, Validation, Supervision, Software, Resources, Project administration, Methodology, Investigation, Funding acquisition, Formal analysis, Data curation, Conceptualization.

## Declaration of competing interest

The authors declare that they have no known competing financial interests or personal relationships that could have appeared to influence the work reported in this paper.

## Acknowledgments

This research was funded by the National Research, Development and Innovation Office (NKFIH) in Hungary through the Grants Nr. K-146181, K-143216, K-134258 and PD-146479. The work in the frame of the 20FUN02 “POLight” project has received funding from the EMPIR programme co-financed by the Participating States and from the European Union’s Horizon 2020 research and innovation programme. Project no. TKP2021-EGA04 has been implemented with support from the Ministry of Innovation and Technology of Hungary from the National Research, Development and Innovation Fund, financed under the TKP2021 funding scheme. On behalf of the ‘MFA-Fotonika-1’ project, we are grateful for the possibility of using HUN-REN Cloud [83]. Project no. C1792954 has been implemented with support from the Ministry of Culture and Innovation of Hungary from the National Research Development and Innovation Fund, financed under the KDP-2021 funding scheme. AP acknowledges the János Bolyai Research Scholarship from the Hungarian Academy of Sciences.

## Appendix A. Supplementary data

Supplementary material related to this article can be found online at https://doi.org/10.1016/j.snb.2024.136875.

## Data availability

Data will be made available on request.

## References

[1] C. Wadell, S. Syrenova, C. Langhammer, Plasmonic hydrogen sensing with nanostructured metal hydrides, ACS Nano 8 (2014) 11925.
[2] N.G. Khlebtsov, L. Lin, B.N. Khlebtsov, J. Ye, Gap-enhanced Raman tags: fabrication, optical properties, and theranostic applications, Theranostics 10 (2020) 2067.
[3] J.J. Baumberg, Hot electron science in plasmonics and catalysis: what we argue about, Faraday Discuss. 214 (2019) 501.
[4] H. Reddy, K. Wang, Z. Kudyshev, L. Zhu, S. Yan, A. Vezzoli, S.J. Higgins, V. Gavini, A. Boltasseva, P. Reddy, V.M. Shalaev, E. Meyhofer, Determining plasmonic hot-carrier energy distributions via single-molecule transport measurements, Science 369 (2020) 423.
[5] J. Budai, Z. Pápa, P. Petrik, P. Dombi, Ultrasensitive probing of plasmonic hot electron occupancies, Nature Commun. 13 (2022) 6695.
[6] A. Carattino, M. Caldarola, M. Orrit, Gold nanoparticles as absolute nanothermometers, Nano Lett. 18 (2018) 874.
[7] G. Baffou, F. Cichos, R. Quidant, Applications and challenges of thermoplasmonics, Nature Mater. 19 (2020) 946.
[8] K. Kawaguchi, S. Yamamoto, M. Yoshikawa, K. Takahiro, Plasmonic cyclohexane-sensing by sputter-deposited Au nanoparticle array on $SiO_2$, Thin Solid Films 562 (2014) 648.
[9] Y. Wang, D.-B. Xiong, W. Zhang, H. Su, Q. Liu, J. Gu, S. Zhu, D. Zhang, Surface plasmon resonance of gold nanocrystals coupled with slow-photon-effect of biomorphic $TiO_2$ photonic crystals for enhanced photocatalysis under visible-light, Catal. Today 274 (2016) 15.
[10] R.S. Moirangthem, Y.-C. Chang, P.-K. Wei, Ellipsometry study on gold-nanoparticle-coated gold thin film for biosensing application, Biomed. Opt. Express (2011) 2569.
[11] S. Kim, S. Park, S. Park, C. Lee, Acetone sensing of Au and Pd-decorated $WO_3$ nanorod sensors, Sensors Actuators B 209 (2015) 180.
[12] H. Yu, Y. Peng, Y. Yang, Z.-Y. Li, Plasmon-enhanced light–matter interactions and applications, npj Comput. Mater. 5 (2019) 45.
[13] J. Homola, Present and future of surface plasmon resonance biosensors, Anal. Bioanal. Chem. 377 (2003) 528.
[14] F. Abelès, Surface electromagnetic waves ellipsometry, Surf. Sci. 56 (1976) 237.
[15] J. Nador, B. Kalas, A. Saftics, E. Agocs, P. Kozma, L. Korosi, I. Szekacs, M. Fried, R. Horvath, P. Petrik, Plasmon-enhanced two-channel in situ Kretschmann ellipsometry of protein adsorption, cellular adhesion and polyelectrolyte deposition on titania nanostructures, Opt. Express 24 (2016) 4812.
[16] A. Bonyár, I. Csarnovics, M. Veres, L. Himics, A. Csik, J. Kámán, L. Balázs, S. Kökényesi, Investigation of the performance of thermally generated gold nanoislands for LSPR and SERS applications, Sensors Actuators B 255 (2018) 433.
[17] D. Zámbó, D.P. Szekrényes, S. Pothorszky, N. Nagy, A. Deák, SERS activity of reporter-particle-loaded single plasmonic nanovoids, J. Phys. Chem. C 122 (2018) 23683.
[18] N.J. Halas, Spiers Memorial Lecture : Introductory lecture: Hot-electron science and microscopic processes in plasmonics and catalysis, Faraday Discuss. (2019) 13.
[19] M.L. Brongersma, N.J. Halas, P. Nordlander, Plasmon-induced hot carrier science and technology, Nature Nanotechnology 10 (2015) 25.
[20] F. Binkowski, T. Wu, P. Lalanne, S. Burger, A.O. Govorov, Hot electron generation through near-field excitation of plasmonic nanoresonators, ACS Photonics 8 (2021) 1243.
[21] D. Gkogkou, T. Shaykhutdinov, T.W. Oates, U. Gernert, B. Schreiber, S. Facsko, P. Hildebrandt, I.M. Weidinger, N. Esser, K. Hinrichs, Characterization of anisotropically shaped silver nanoparticle arrays via spectroscopic ellipsometry supported by numerical optical modeling, Appl. Surf. Sci. 421 (2017) 460.
[22] N. Cioffi, L. Torsi, I. Farella, D. Altamura, A. Valentini, N. Ditaranto, L. Sabbatini, P.G. Zambonin, T. Bleve-Zacheo, Deposition and analytical characterization of fluoropolymer thin films modified by palladium nanoparticles, Thin Solid Films 449 (2004) 25.
[23] G. Kumar, X. Li, Y. Du, Y. Geng, X. Hong, UV-light enhanced high sensitive hydrogen ($H_2$) sensor based on spherical Au nanoparticles on ZnO nano-structured thin films, J. Alloys Compd. 798 (2019) 467.
[24] R. Borah, J. Smets, R. Ninakanti, M.L. Tietze, R. Ameloot, D.N. Chigrin, S. Bals, S. Lenaerts, S.W. Verbruggen, Self-assembled ligand-capped plasmonic Au nanoparticle films in the kretschmann configuration for sensing of volatile organic compounds, ACS Appl. Nano Mater. 5 (2022) 11494.
[25] J.N. Anker, W.P. Hall, O. Lyandres, N.C. Shah, J. Zhao, R.P. Van Duyne, Biosensing with plasmonic nanosensors, Nature Mater. 7 (2008) 442.
[26] N. Mandal, A. Das, R.S. Moirangthem, In-situ label-free optical biosensing with plasmonic enhanced ellipsometry using partially-embedded bimetallic Ag-Au alloy nanoparticles, Sensors Actuators B 379 (2023) 133164.

[27] G. Sirinakis, R. Sun, R. Siddique, H. Efstathiadis, M.A. Carpenter, A.E. Kaloyeros, Synthesis and spectroellipsometric characterization of $Y_2O_3$-stabilized $ZrO_2$-Au nanocomposite films for smart sensor applications, 846, 2005, p. 269,

[28] W.-H. Tsai, K. cherng Lin, S. Yang, Y.-C. Tsao, P. Ho, Fiber-optic surface plasmon resonance-based sensor with AZO/Au bilayered sensing layer, Chin. Opt. Lett. 12 (2014) 042801.

[29] D.I. Meira, R.P. Domingues, M.S. Rodrigues, E. Alves, N.P. Barradas, J. Borges, F. Vaz, Thin films of Au-$Al_2O_3$ for plasmonic sensing, Appl. Surf. Sci. 500 (2020) 144035.

[30] N.M. Figueiredo, F. Vaz, L. Cunha, A. Cavaleiro, Au-$WO_3$ nanocomposite coatings for localized surface plasmon resonance sensing, Materials 13 (2020) 13010246.

[31] M. Saini, S. Augustine, M. Ranjan, T. Som, In-plane optical anisotropy and SERS detection efficiency of self-organized gold nanoparticles on silicon nanoripples: Roles of growth angle and postgrowth annealing, Appl. Surf. Sci. 512 (2020) 145703.

[32] E.G. Bortchagovsky, in: M. Pluta, T.R. Wolinski (Eds.), Possibilities of Ellipsometry with Surface Plasmon Excitation in the Investigation of Thin Films in Comparison to Separated Ellipsometry and Surface Plasmon Spectroscopy, Kazimierz Dolny, Poland, 1997, p. 239.

[33] X. Liu, Q. Dai, L. Austin, J. Coutts, G. Knowles, J. Zou, H. Chen, Q. Huo, A one-step homogeneous immunoassay for cancer biomarker detection using gold nanoparticle probes coupled with dynamic light scattering, J. Am. Chem. Soc. 130 (2008) 2780.

[34] X. Huang, R. O'Connor, E.A. Kwizera, Gold nanoparticle based platforms for circulating cancer marker detection, Nanotheranostics 1 (2017) 80.

[35] A. Atapour, H. Khajehzadeh, M. Shafie, M. Abbasi, S. Mosleh-Shirazi, S.R. Kasaee, A.M. Amani, Gold nanoparticle-based aptasensors: A promising perspective for early-stage detection of cancer biomarkers, Mater. Today Commun. 30 (2022) 103181.

[36] R. Thiramanas, R. Laocharoensuk, Competitive binding of polyethyleneimine-coated gold nanoparticles to enzymes and bacteria: a key mechanism for low-level colorimetric detection of gram-positive and gram-negative bacteria, Microchim. Acta 183 (2016) 389.

[37] X. Yang, Y. Dang, J. Lou, H. Shao, X. Jiang, D-alanyl-D-alanine-modified gold nanoparticles form a broad-spectrum sensor for bacteria, Theranostics 8 (2018) 1449.

[38] G. Landa, L.G. Miranda-Calderon, V. Sebastian, S. Irusta, G. Mendoza, M. Arruebo, Selective point-of-care detection of pathogenic bacteria using sialic acid functionalized gold nanoparticles, Talanta 234 (2021) 122644.

[39] R.V. Nair, T. Thomas, H. Kuttoth, A. Karthikeyan, B.G. Nair, N. Sandhyarani, $Cu^{2+}$-mediated aggregation of gold nanoparticles as an optical probe for the detection of endotoxin, Langmuir 38 (2022) 10826.

[40] V. Amendola, R. Pilot, M. Frasconi, O.M. Maragò, M.A. Iatì, Surface plasmon resonance in gold nanoparticles: A review, J. Phys.: Condens. Matter. 29 (2017) 203002.

[41] S.-f. Liu, Y.-f. Li, J.-r. Li, L. Jiang, Enhancement of DNA immobilization and hybridization on gold electrode modified by nanogold aggregates, Biosens. Bioelectron. 21 (2005) 789.

[42] K.M. McPeak, S.V. Jayanti, S.J.P. Kress, S. Meyer, S. Iotti, A. Rossinelli, D.J. Norris, Plasmonic films can easily be better: Rules and recipes, ACS Photonics 2 (2015) 326.

[43] B. Kalas, J. Nador, E. Agocs, A. Saftics, S. Kurunczi, M. Fried, P. Petrik, Protein adsorption monitored by plasmon-enhanced semi-cylindrical Kretschmann ellipsometry, Appl. Surf. Sci. 421 (2017) 585.

[44] B. Kalas, K. Ferencz, A. Saftics, Z. Czigany, M. Fried, P. Petrik, Bloch surface waves biosensing in the ultraviolet wavelength range – Bragg structure design for investigating protein adsorption by in situ Kretschmann-Raether ellipsometry, Appl. Surf. Sci. 536 (2021) 147869.

[45] B. Kalas, G. Sáfrán, M. Serényi, M. Fried, P. Petrik, Scanning-resonance optical sensing based on a laterally graded plasmonic layer—optical properties of $Ag_xAl_{1-x}$ in the range of $x = 0$ to 1, Appl. Surf. Sci. 606 (2022) 154770.

[46] C. Carnegie, R. Chikkaraddy, F. Benz, B. De Nijs, W.M. Deacon, M. Horton, W. Wang, C. Readman, S.J. Barrow, O.A. Scherman, J.J. Baumberg, Mapping SERS in CB:Au plasmonic nanoaggregates, ACS Photonics 4 (2017) 2681.

[47] A. Kosinova, D. Wang, E. Baradács, B. Parditka, T. Kups, L. Klinger, Z. Erdélyi, P. Schaaf, E. Rabkin, Tuning the nanoscale morphology and optical properties of porous gold nanoparticles by surface passivation and annealing, Acta Mater. 127 (2017) 108.

[48] M.V. Sosnova, N.L. Dmitruk, A.V. Korovin, S.V. Mamykin, V.I. Mynko, O.S. Lytvyn, Local plasmon excitations in one-dimensional array of metal nanowires for sensor applications, Appl. Phys. B 99 (2010) 493.

[49] E.S. Kooij, H. Wormeester, E.A.M. Brouwer, E. van Vroonhoven, A. van Silfhout, B. Poelsema, Optical characterization of thin colloidal gold films by spectroscopic ellipsometry, Langmuir 18 (2002) 4401.

[50] E. Brouwer, E. Kooij, M. Hakbijl, H. Wormeester, B. Poelsema, Deposition kinetics of nanocolloidal gold particles, Colloids Surf. A 267 (2005) 133.

[51] R.S. Moirangthem, M.T. Yaseen, P.-K. Wei, J.-Y. Cheng, Y.-C. Chang, Enhanced localized plasmonic detections using partially-embedded gold nanoparticles and ellipsometric measurements, Biomed. Opt. Express 3 (2012) 899.

[52] E. Martinsson, M.A. Otte, M.M. Shahjamali, B. Sepulveda, D. Aili, Substrate effect on the refractive index sensitivity of silver nanoparticles, J. Phys. Chem. C 118 (2014) 24680.

[53] J. Olesiak-Banska, M. Waszkielewicz, P. Obstarczyk, M. Samoc, Two-photon absorption and photoluminescence of colloidal gold nanoparticles and nanoclusters, Chem. Soc. Rev. 48 (2019) 4087.

[54] R.W. Taylor, T.-C. Lee, O.A. Scherman, R. Esteban, J. Aizpurua, F.M. Huang, J.J. Baumberg, S. Mahajan, Precise subnanometer plasmonic junctions for SERS within gold nanoparticle assemblies using cucurbit[n]uril "glue", ACS Nano 5 (2011) 3878.

[55] A. Deák, B. Bancsi, A. Tóth, A. Kovács, Z. Hórvölgyi, Complex Langmuir-Blodgett films from silica nanoparticles: An optical spectroscopy study, Colloids Surf. A 278 (2006) 10.

[56] P. Kozma, B. Fodor, A. Deak, P. Petrik, Optical models for the characterization of silica nanosphere monolayers prepared by the Langmuir-Blodgett method using ellipsometry in the quasistatic regime, Langmuir 26 (2010) 16122.

[57] Y. Ke, X. Wen, D. Zhao, R. Che, Q. Xiong, Y. Long, Controllable fabrication of two-dimensional patterned $VO_2$ nanoparticle, nanodome, and nanonet arrays with tunable temperature-dependent localized surface plasmon resonance, ACS Nano 11 (2017) 7542.

[58] O. Bialas, M. Lis, A. Woźniak, M. Adamiak, Laser superficial fusion of gold nanoparticles with PEEK polymer for cardiovascular application, Materials 14 (2021).

[59] L.-W. Hu, X. Liu, G.-M. Le, J.-F. Li, F.-S. Qu, S.-Y. Lu, L. Qi, Morphology evolution and SERS activity of the nanoporous Au prepared by dealloying sputtered Au-Ag film, Physica B 558 (2019) 49.

[60] G.G. Politano, E. Cazzanelli, C. Versace, C. Vena, M.P. De Santo, M. Castriota, F. Ciuchi, R. Bartolino, Graphene oxide on magnetron sputtered silver thin films for SERS and metamaterial applications, Appl. Surf. Sci. 427 (2018) 927.

[61] H. Bakkali, E. Blanco, M. Domínguez, J.S. Garitaonandia, Fabrication and optical properties of nanostructured plasmonic $Al_2O_3$/Au–$Al_2O_3$/$Al_2O_3$ metamaterials, Nanotechnology 28 (2017) 335704.

[62] L. Armelao, D. Barreca, G. Bottaro, G. Bruno, A. Gasparotto, M. Losurdo, E. Tondello, RF-sputtering of gold on silica surfaces: Evolution from clusters to continuous films, Mater. Sci. Eng. C 25 (2005) 599.

[63] L. Juhász, B. Parditka, P. Petrik, C. Cserháti, Z. Erdélyi, Continuous tuning of the plasmon resonance frequency of porous gold nanoparticles by mixed oxide layers, J. Porous Mater. 27 (2020) 1583.

[64] A. Serrano, O. Rodriguez De La Fuente, M. García, Extended and localized surface plasmons in annealed Au films on glass substrates, J. Appl. Phys. 108 (2010) 074303.

[65] E. Kretschmann, H. Raether, Radiative decay of non radiative surface plasmons excited by light, Z. Naturforsch. A 23 (12) (1968) 2135.

[66] T. Oates, H. Wormeester, H. Arwin, Characterization of plasmonic effects in thin films and metamaterials using spectroscopic ellipsometry, Prog. Surf. Sci. (2011) 328.

[67] T.W.H. Oates, H. Sugime, S. Noda, Combinatorial surface-enhanced Raman spectroscopy and spectroscopic ellipsometry of silver island films, J. Phys. Chem. C (2009) 4820.

[68] N. Dmitruk, O. Mayeva, S. Mamykin, O. Yastrubchak, M. Klopfleisch, Characterization and application of multilayer diffraction gratings as optochemical sensors, Sensors Actuators A (2001) 52.

[69] H.T. Beyene, J.W. Weber, M.A. Verheijen, M.C.M. Van De Sanden, M. Creatore, Real time in situ spectroscopic ellipsometry of the growth and plasmonic properties of au nanoparticles on $SiO_2$, Nano Res. 5 (2012) 513.

[70] G. Sáfrán, "One-sample concept" micro-combinatory for high throughput TEM of binary films, Ultramicroscopy 187 (2018) 50.

[71] B. Kalas, Z. Zolnai, G. Sáfrán, M. Serényi, E. Agocs, T. Lohner, A. Nemeth, N.Q. Khánh, M. Fried, P. Petrik, Micro-combinatorial sampling of the optical properties of hydrogenated amorphous $Si_{1-x}Ge_x$ for the entire range of compositions towards a database for optoelectronics, Sci. Rep. 10 (2020) 19266.

[72] M. Loncaric, J. Sancho-Parramon, H. Zorc, Optical properties of gold island films—a spectroscopic ellipsometry study, Thin Solid Films 519 (2011) 2946.

[73] F.A.A. Nugroho, B. Iandolo, J.B. Wagner, C. Langhammer, Bottom-up nanofabrication of supported noble metal alloy nanoparticle arrays for plasmonics, ACS Nano 10 (2016) 2871.

[74] G. Piszter, K. Kertész, Z. Bálint, L.P. Biró, Optical detection of vapor mixtures using structurally colored butterfly and moth wings, Sensors 19 (14) (2019) 3058.

[75] R. Synowicki, C.M. Herzinger, J.T. Hall, A. Malingowski, Optical constants of electroplated gold from spectroscopic ellipsometry, Appl. Surf. Sci. 421 (2017) 824.

[76] X. Wang, K.-P. Chen, M. Zhao, D. Nolte, Refractive index and dielectric constant evolution of ultra-thin gold from clusters to films, Opt. Express 18 (2010) 24859.
[77] M. Kang, S.-G. Park, K.-H. Jeong, Repeated solid-state dewetting of thin gold films for nanogap-rich plasmonic nanoislands, Sci. Rep. 5 (2015) 14790.
[78] K.L. Kelly, E. Coronado, L.L. Zhao, G.C. Schatz, The optical properties of metal nanoparticles: The influence of size, shape, and dielectric environment, J. Phys. Chem. B 107 (2003) 668.
[79] J. Katyal, R. Soni, Size- and shape-dependent plasmonic properties of aluminum nanoparticles for nanosensing applications, J. Modern Opt. 60 (2013) 1717.
[80] G. Kewes, F. Binkowski, S. Burger, L. Zschiedrich, O. Benson, Heuristic modeling of strong coupling in plasmonic resonators, ACS Photonics 5 (2018) 4089.
[81] Z. Osváth, A. Deák, K. Kertész, G. Molnár, G. Vértesy, D. Zámbó, C. Hwang, L.P. Biró, The structure and properties of graphene on gold nanoparticles, Nanoscale 7 (2015) 5503.
[82] W. Chen, S. Zhang, M. Kang, W. Liu, Z. Ou, Y. Li, Y. Zhang, Z. Guan, H. Xu, Probing the limits of plasmonic enhancement using a two-dimensional atomic crystal probe, Light: Sci. Appl. 7 (2018) 56.
[83] M. Héder, E. Rigó, D. Medgyesi, R. Lovas, S. Tenczer, F. Török, A. Farkas, M. Emődi, J. Kadlecsik, G. Mező, Á. Pintér, P. Kacsuk, The past, present and future of the ELKH cloud, Inf. Társadalom 22 (2) (2022) 128.

**Deshabrato Mukherjee** is a Ph.D. student in the Photonics Laboratory of the HUN-REN EK MFA. He is working on the development of optical characterization techniques.

**Krisztián Kertész** is a senior researcher in the Nanostructures Laboratory of the HUN-REN EK MFA. He is working on the development of optical characterization tools.

**Zsolt Zolnai** is a senior researcher in the Nanosensors Laboratory of the HUN-REN EK MFA. He is working on ion beam analysis and optical evaluations.

**Zoltán Kovács** received his master degree from the Eötvös Loránd University. He was responsible for optical measurements and evaluations.

**András Deák** is a scientific advisor in the Photonics Laboratory of the HUN-REN EK MFA and the head of the group of Chemical Nanostructures. His scientific interest includes the preparation and spectroscopy of colloid nanoparticles.

**András Pálinkás** is a senior researcher in the Nanostructures Laboratory of the HUN-REN EK MFA. He is working on scanning probe methods and Raman spectroscopy.

**Zoltán Osváth** is a senior researcher in the Nanostructures Laboratory of the HUN-REN EK MFA. He is working on scanning probe methods and Raman spectroscopy.

**Dániel Olasz** is a Ph.D. student in the Thin Film Physics Laboratory of the HUN-REN EK MFA. He is working on magnetron sputtering methods.

**Alekszej Romanenko** is a Ph.D. student in the Photonics Department of the HUN-REN EK MFA. He is working on optical measurements and evaluations.

**Miklós Fried** is a scientific advisor in the Photonics Department of the HUN-REN EK MFA. He is working on optical measurements and evaluations.

**Sven Burger** is a member of the Computational Nano-Optics group and of the spin-off company JCMwave GmbH. He is working on finite element methods for optical evaluations.

**György Sáfrán** is a scientific advisor in the Thin Film Physics Laboratory of the HUN-REN EK MFA. He is working on magnetron sputtering methods.

**Peter Petrik** is the head of the Photonics Laboratory of the HUN-REN EK MFA. He is working on optical measurements and evaluations.